Framework for computing the spatial coherence effects of polycapillary x-ray optics

Adam M. Zysk,[1] **Robert W. Schoonover,**[2] **Qiaofeng Xu,**[2] **and Mark A. Anastasio**[2,*]

[1]*Department of Biomedical Engineering, Medical Imaging Research Center, Illinois Institute of Technology, 3440 South Dearborn Street, Suite 100, Chicago, Illinois 60616, USA*
[2]*Department of Biomedical Engineering, Washington University in St. Louis, Whitaker Hall, Campus Box 1097, One Brookings Drive, St. Louis, Missouri, 63130, USA*

[*]*anastasio@seas.wustl.edu*

Abstract: Despite the extensive use of polycapillary x-ray optics for focusing and collimating applications, there remains a significant need for characterization of the coherence properties of the output wavefield. In this work, we present the first quantitative computational method for calculation of the spatial coherence effects of polycapillary x-ray optical devices. This method employs the coherent mode decomposition of an extended x-ray source, geometric optical propagation of individual wavefield modes through a polycapillary device, output wavefield calculation by ray data resampling onto a uniform grid, and the calculation of spatial coherence properties by way of the spectral degree of coherence.

© 2012 Optical Society of America

OCIS codes: (030.1640) Coherence; (340.0340) X-ray optics.

References and links

1. C. Schroer and B. Lengeler, "X-ray optics," in *Springer Handbook of Lasers and Optics*, F. Träger, ed., (Springer-Verlag, 2007).
2. C. A. MacDonald and W. M. Gibson, "Applications and advances in polycapillary optics," X-ray Spectrom. **32**, 258–268 (2003).
3. Yu. M. Alexandrov, S. B. Dabagov, M. A. Kumakhov, V. A. Murashova, D. A. Fedin, R. V. Fedorchuk, and M. N. Yakimenko, "Peculiarities of photon transmission through capillary systems," Nucl. Instrum. Methods Phys. Res., Sect. B **134**, 174–180 (1998).
4. S. B. Dabagov and A. Marcelli, "Single-reflection regime of x rays that travel into a monocapillary," Appl. Opt. **38**, 7494–7497 (1999).
5. S. V. Kukhlevsky, F. Flora, A. Marinai, G. Nyitray, Zs. Kozma, A. Ritucci, L. Palladino, A. Reale, and G. Tomassetti, "Wave-optics treatment of x-rays passing through tapered capillary guides," X-Ray Spectrom. **29**, 354–359 (2000).
6. S. B. Dabagov, "Wave theory of x-ray scattering in capillary structures," X-Ray Spectrom. **32**, 223–228 (2003).
7. L. Vincze, K. Janssens, F. Adams, and A. Rindby, "Detained ray-tracing code for capillary optics," X-Ray Spectrom. **24**, 27-37 (1995).
8. S. V. Kukhlevsky, F. Flora, A. Marinai, G. Nyitray, A. Ritucci, L. Palladino, A. Reale, and G. Tomassetti, "Diffraction of X-ray beams in capillary waveguides," Nucl. Instrum. Methods Phys. Res., Sect. B **168**, 276–282 (2000).
9. S. V. Kukhlevsky, "Interference and diffraction in capillary x-ray optics," X-Ray Spectrom. **32**, 223–228 (2003).
10. Q. F. Xiao and S. V. Poturaev, "Polycapillary-based X-ray optics," Nucl. Instrum. Methods Phys. Res., Sect. A **347**, 376–383 (1994).
11. A. Liu, "The X-ray distribution after a focussing polycapillary a shadow simulation," Nucl. Instrum. Methods Phys. Res., Sect. B **243**, 223–226 (2006).

12. C. Welnak, G. J. Chen, and F. Cerrina, "Shadow: a synchrotron radiation and X-ray optics simulation tool," Nucl. Instrum. Methods Phys. Res., Sect. A **347**, 344–347 (1994).
13. D. Hampai, S. B. Dabagov, G. Cappuccio, and G. Cibin, "X-ray propagation through hollow channel: PolyCAD - a ray tracing code," Nucl. Instrum. Methods Phys. Res., Sect. B **244**, 481–488 (2006).
14. D. Hampai, S. B. Dabagov, G. Cappuccio, and G. Cibin, "X-ray propagation through polycapillary optics studied through a ray tracing approach," Spectrochim. Acta, Part B **62**, 608–614 (2007).
15. S. B. Dabagov, M. A. Kumakhov, S. V. Nikitina, V. A. Murashova, R. V. Fedorchuk, and M. N. Yakimenko, "Observation of interference effects at the focus of an x-ray lens," J. Synchrotron Radiat. **2**, 132–135 (1995).
16. S. B. Dabagov, M. A. Kumakhov, and S. V. Nikitina, "On the interference of X-rays in multiple reflection optics," Phys. Lett. A **203**, 279–282 (1995).
17. A. Bjeoumikhov, "Observation of peculiarities in angular distributions of X-ray radiation after propagation through polycapillary structures," Phys. Lett. A **360**, 405–410 (2007).
18. A. Bjeoumikhov, S. Bjeoumikhova, H. Riesemeier, M. Radtke, and R. Wedell, "Propagation of synchrotron radiation through nanocapillary structures," Phys. Lett. A **366**, 283–288 (2007).
19. S. B. Dabagov, R. V. Fedorchuk, V. A. Murashova, S. V. Nikitina, and M. N. Yakimenko, "Interference phenomenon under focusing of synchrotron radiation by a Kumakhov lens," Nucl. Instrum. Methods Phys. Res., Sect. B **108**, 213-218 (1996).
20. L. Vincze, K. Janssens, and S. V. Kukhlevsky, "Simulation of polycapillary lenses for coherent and partially coherent x-rays," Proc. SPIE **5536**, 81–85 (2004).
21. L. Mandel and E. Wolf, *Optical Coherence and Quantum Optics* (Cambridge University Press, 1995).
22. E. Wolf, "New spectral representation of random sources and of the partially coherent field that they generate," Opt. Commun. **38**, 3–6 (1981).
23. H. Liu, G. Mu, and L. Lin, "Propagation theories of partially coherent electromagnetic fields based on coherent or separated-coordinate mode decomposition," J. Opt. Soc. Am. A **23**, 2208–2218 (2006).
24. A. M. Zysk, P. S. Carney, and J. C. Schotland, "Eikonal method for calculation of coherence functions," Phys. Rev. Lett. **95**, 043904 (2005).
25. R. W. Schoonover, A. M. Zysk, and P. S. Carney, "Geometrical optics limit of stochastic electromagnetic fields," Phys. Rev. A **77**, 043831 (2008).
26. A. Liu, "Simulation of x-ray propagation in a straight capillary," Math. Comput. Simulat. **65**, 251–256 (2004).
27. A. Liu, "Simulation of x-ray beam collimation by polycapillaries," Nucl. Instrum. Methods Phys. Res., Sect. B **234**, 555–562 (2005).
28. Q. Xiao, I. Ponomarev, A. Kolomitsev, and J. Kimball, "Numerical simulations for capillary-based x-ray optics," Proc. SPIE **1736**, 227–238 (1992).
29. M. Popov, "A new method of computation of wave fields using gaussian beams," Wave Motion **4**, 85–97 (1982).
30. A. Norris, "Complex point-source representation of real point sources and the gaussian beam summation method," J. Opt. Soc. Am. A **3**, 2005–2010 (1986).
31. G. Forbes and M. Alonso, "Using rays better. I. theory for smoothly varying media," J. Opt. Soc. Am. A **18**, 1132–1145 (2001).
32. T. Heilpern, E. Heyman, and V. Timchenko, "A beam summation algorithm for wave radiation and guidance in stratified media," J. Acoust. Soc. Am. **121**, 1856–1864 (2007).
33. E. Svensson, "Gaussian beam summation in shallow waveguides," Wave Motion **45**, 445–456 (2008).
34. J. Jackson, C. Meyer, D. Nishimura, and A. Macovski, "Selection of a convolution function for fourier inversion using gridding [computerised tomography application]," IEEE Trans. Med. Imag. **10**, 473–478 (1991).
35. S. Bollanti, P. Albertano, M. Belli, P. Di Lazzaro, A. Ya. Faenov, F. Flora, G. Giordano, A. Grilli, F. Ianzinni, S. V. Kukhlevsky, T. Letardi, A. Nottola, L. Palladino, T. Pikuz, A. Reale, L. Reale, A. Scafati, M. A. Tabocchini, I. C. E. Turcu, K. Vigli-Papadaki, and G. Schina, "Soft X-ray plasma source for atmospheric-pressure microscopy, radiobiology and other applications," Il Nuovo Cimento **20**, 1685–1701 (1998).
36. B. Hargreaves and P. Beatty, "Gridding functions," http://mrsrl.stanford.edu/ brian/gridding/.
37. D. Hampai, S. B. Dabagov, G. Cappuccio, G. Cibin, and V. Sessa, "X-ray micro-imaging by capillary optics," Spectrochim. Acta, Part B **64**, 1180–1184 (2009).

1. Introduction

The use of x-ray optics in imaging studies has taken on a vital role in the synchrotron and laboratory communities [1, 2]. Polycapillary devices, also known as Kumakhov lenses, consist of collections of glass capillaries that direct x-rays by total external reflection to focus or collimate the output. Coherence effects are well known to exist in capillary structures, as a number of wave theory-based investigations have demonstrated the simulation of x-ray propagation through single capillary devices, usually with synchrotron or soft x-ray laser illumination, and the presence of diffraction and interference effects in the output wavefield [3–6]. As the capil-

lary device size is typically large relative to the wavelength, these simulations have generally relied on geometrical optics or Fresnel-Kirchoff approximations [7–9].

Many simulation studies of polycapillary devices [10] are also performed with ray-tracing toolboxes such as SHADOW [11, 12] and PolyCAD [13, 14]. These simulations function by computing the paths of x-rays through a device and evaluating the number of rays incident on each pixel in the output plane as an estimate of the output intensity. Importantly, the intensity estimate found with these techniques is not directly derived from the underlying wavefield and therefore neglects intensity modulations due to interference effects.

Although diffraction and interference effects in single capillary devices have been extensively investigated experimentally [15–18] and in simulation, relatively little is known of the changes in spatial coherence brought about by propagation through polycapillary devices, especially in the presence of extended laboratory sources [19, 20]. Access to the wavefield data after propagation through the device is necessary for analysis of these effects. In this paper, we present the first demonstration of a method to simulate the wavefield data at the output of a polycapillary device due to an extended source and analyze the resulting spatial coherence properties without the need for an analytically tractable wave-based representation of the optic.

2. Methods

2.1. Coherence theory

Statistical optics, or coherence theory, describes observable phenomena for non-deterministic optical wavefields [21]. The coherence properties of wavefields generated by a statistically stationary optical source, $\tilde{U}_s(\mathbf{r},t)$, are characterized by the autocorrelation function, $\Gamma_s(\mathbf{r}_1,\mathbf{r}_2,\tau) = \langle \tilde{U}_s^*(\mathbf{r}_1,t)\tilde{U}_s(\mathbf{r}_2,t+\tau)\rangle$, where the angle brackets denote an ensemble average over realizations of the source, and tildes indicate random variables. The corresponding cross-spectral density is defined as $W_s(\mathbf{r}_1,\mathbf{r}_2,\omega) = \int d\tau \Gamma_s(\mathbf{r}_1,\mathbf{r}_2,\tau)e^{i\omega\tau}$, where ω is the temporal frequency. The cross-spectral density of stochastic, extended sources is Hermitian and thus has a Mercer expansion, or coherent mode decomposition (CMD) [22],

$$W_s(\mathbf{r}_1,\mathbf{r}_2,\omega) = \sum_{n=1}^{\infty} \beta_n(\omega)\phi_n^*(\mathbf{r}_1,\omega)\phi_n(\mathbf{r}_2,\omega), \tag{1}$$

where * indicates complex conjugation. Here, the cross-spectral density is equal to the incoherent sum of statistically independent modes, $\phi_n(\mathbf{r},\omega)$, each weighted by a quantity $\beta_n(\omega)$.

It can be readily shown that the cross-spectral density for a stochastic wavefield $\tilde{U}(\mathbf{r},\omega)$, which is the propagated wavefield $\tilde{U}_s(\mathbf{r},\omega)$, is given by

$$\begin{aligned} W(\mathbf{r}_1,\mathbf{r}_2,\omega) &= \langle \tilde{U}^*(\mathbf{r}_1,\omega)\tilde{U}(\mathbf{r}_2,\omega)\rangle \\ &= \sum_{n=1}^{\infty} \beta_n(\omega)\psi_n^*(\mathbf{r}_1,\omega)\psi_n(\mathbf{r}_2,\omega), \end{aligned} \tag{2}$$

where $\psi_n(\mathbf{r},\omega)$ are found by propagating $\phi_n(\mathbf{r},\omega)$. That is, the cross-spectral density of a propagated wavefield is the incoherent sum of the propagated modes of the wavefield at the source, multiplied by the original weights $\beta_n(\omega)$. The propagated modes can be found via the method of Green functions [23], computational methods, or geometrical optics [24, 25].

Finally, the spectral degree of coherence, which quantifies the degree of statistical similarity between the wavefield at two points in space, is defined

$$\mu(\mathbf{r}_1,\mathbf{r}_2,\omega) = \frac{W(\mathbf{r}_1,\mathbf{r}_2,\omega)}{\sqrt{W(\mathbf{r}_1,\mathbf{r}_1,\omega)W(\mathbf{r}_2,\mathbf{r}_2,\omega)}}. \tag{3}$$

When $|\mu(\mathbf{r}_1,\mathbf{r}_2,\omega)| = 1$, the wavefield is fully coherent between the two points. When $|\mu(\mathbf{r}_1,\mathbf{r}_2,\omega)| = 0$, the wavefield is completely incoherent between the two points.

In this work, we introduce and demonstrate a method for the calculation of the spectral degree of coherence for a wavefield that has propagated through a polycapillary device. This method consists of the following steps: (1) The spatially partially-coherent anode source is decomposed into a collection of statistically-independent point sources that are interpreted as the modes $\phi_n(\mathbf{r},\omega)$ in Eq. (1). (2) The wavefield from each point source, or mode, is propagated through the polycapillary device using geometrical ray tracing. (3) The wavefield on the output plane is constructed by combining and resampling the ray data. (4) The wavefield from the output plane is optionally propagated away from the polycapillary device. (5) The spectral degree of coherence is computed by way of the CMD in Eq. (2).

2.2. Modeling an extended source and polycapillary device

In this section, we show an implementation of this method in which an x-ray tube source and collimating polycapillary optic are modeled. In step 1, an x-ray tube source anode is modeled by a collection of incoherent point emitters with a Gaussian spatial profile. In the CMD representation, the modes and weights are of the form $\phi_n(\mathbf{r},\omega) = \delta(\mathbf{r} - \mathbf{r}_n)$ and $\beta_n(\omega) = S(\omega)\exp\left(-r_n^2/2v^2\right)$, where $S(\omega)$ is the spectrum of the anode, v is the radius of the anode spot, and $\mathbf{r}_n$ are the sampled points on the anode. Each source point, or mode, generates a spherical wave centered at $\mathbf{r}_n$. An anode consisting of 49 source points laid out on a rectangular grid with radius $v = 2.1~\mu$m (corresponding to a full-width half maximum value of 5 μm) and maximum radial anode position 6.4 μm is simulated.

In step 2, interaction of individual wavefields, which correspond to coherent modes, with the polycapillary optic is modeled using geometrical optical propagation. In geometrical optics (also known as the high-frequency limit), the propagating wavefield is assumed to be of the form $U(\mathbf{r},\omega) = A(\mathbf{r})\exp[i\omega S(\mathbf{r})/c]$, where $A(\mathbf{r})$, the amplitude, and $S(\mathbf{r})$, the eikonal or optical path length, are independent of frequency, and c is the speed of light.

The polycapillary optic modeled in this work is a collimating optic consisting of 19 curved glass capillaries arranged in a hexagonal pattern on the input and output surfaces. The interior wall of a given capillary is defined by $[x - x_l g_l(z)]^2 + [y - y_l g_l(z)]^2 = r_0^2 f_l^2(z)$, where (x_l, y_l) denote the center of the lth capillary at the input, r_0 is the radius of the capillary at the input, and $f_l(z)$ and $g_l(z)$ are second-order polynomials in z chosen such that the capillary input face is normal to the device input focus location and the capillary exit plane is normal to the optical axis [26, 27]. The device modeled in this work consists of glass capillaries with a dielectric constant $\varepsilon = 1 - 9.115 \times 10^{-6} + i1.145 \times 10^{-7}$ at an energy of 8 keV [28], a capillary input radius of 6 μm, an input focus location 3 cm from the input face, and a polycapillary device length of 23 cm. For each point source, or mode, $N = 1 \times 10^7$ ray trajectories are uniformly randomly angularly distributed to model an outgoing spherical wavefield centered at the point source location. Each ray, labeled m, has initial amplitude $A_m = 1$.

A ray-tracing algorithm finds the capillary, if any, into which each ray enters. Each entering ray has a straight-line trajectory until it intersects a capillary wall at which point Snell's law is used to calculate the new trajectory and the amplitude reflection coefficient R. After each reflection, the ray amplitude is updated $A_m \rightarrow A_m R$. As each ray propagates through the capillary, the ray's eikonal is tabulated. This process continues until the ray has traveled to the exit plane of the capillary. At the end of the computation, the exit plane location, eikonal, and amplitude of each ray is recorded. In this simulation, rays that do not enter a capillary are assumed to be lost from the system and rays are not allowed to move between capillaries.

2.3. Calculation of the output wavefield

In step 3, the wavefield at the polycapillary output is computed by combining and resampling the discrete ray data onto a uniform grid. A number of methods exist to accomplish this task, including Gaussian beam weighting methods from the optical physics community, which have been used to account for the non-uniformity of ray data [29–31] in simulations of a number of system geometries [32, 33]. We have chosen to implement a computationally-efficient weighted beam gridding method, variants of which have been used in the computed tomography community for treatment of non-uniformly sampled spatial Fourier-domain data [34]. In this simulation, the gridding operation is performed by convolving ray point data from each capillary with a Kaiser-Bessel kernel and then sampling on a uniform grid [34].

Specifically, the amplitude and eikonal ray data from each capillary are grouped by the total number of reflections. The gridding routine by Hargreaves and Beatty [36] is applied to each group with a 1024×1024 pixel grid size, a kernel width of 5, and an overgrid factor of 3 as described by Jackson *et al.* [34]. The resulting wavefields from the reflection groups are summed to arrive at a final output wavefield from each capillary and then combined to form a finely-sampled final output wavefield for the entire device due to one anode source point (50 nm pixel spacing). These data, when computed for each anode source point, are the coherent modes, $\psi_n(\mathbf{r}, \omega)$, of the propagated wavefield from the extended source which are combined in step 5 via the CMD in Eq. (2) to compute the spectral degree of coherence in Eq. (3).

2.4. Validation of wavefield generation method

To validate the wavefield generation method used here, the output of a parallel-plane waveguide illuminated by a soft x-ray laser source has been computed for comparison to results by Kukhlevsky, *et al.* [8]. In the previous work, the intensity output of a SiO_2 device (length = 21 cm, plane separation = 300 μm) illuminated by a quasi-monochromatic source ($\lambda = 20$ nm, diameter = 50 μm) [35] at a distance of 78.5 cm was measured at a distance of 33.4 cm from the output and simulated using an approximation method, namely the Fresnel-Kirchoff theory. The field at the output of the device is described as the superposition of m "field modes," where each mode corresponds to the initial field having been reflected m times.
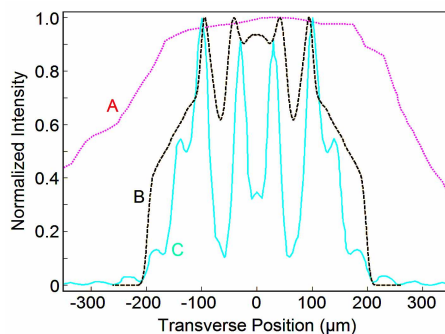

Fig. 1. The transverse intensity response from a parallel-plane waveguide illuminated by a soft x-ray laser source. The simulation results using the techniques in this work (B) are compared to simulated results (C) and experimental measurements (A) from the literature [8]. Portions of this figure are reprinted from Nuclear Instruments and Methods in Physics Reseach B, Vol. 168, S.V. Kukhlevsky, *et al.*, "Diffraction of X-ray beams in capillary waveguides," Pages 276-282, Copyright 2000, with permission from Elsevier.

In Fig. 1, the simulated (labeled C) and experimental (labeled A) results reported in [8,

see Fig. 3(a)] and the simulation results generated with the method described in this work (labeled B) are shown. One notes that both sets of simulation results predict the same peak and trough structure as well as the same approximate width for the output field. In the work by Kukhlevsky *et al.*, the simulated field is reported to be consistent with one in which $m_{max} = 1$. The field produced with the method in this paper also consists of $m_{max} = 1$ reflections. It is also noteworthy that both simulations neglected the polychromaticity of the source [35] and that neither account for the spatial response of the detector.

The two sets of simulated results in Fig. 1 differ in terms of the predcted depth of the troughs. One notes, however, that neither the Fresnel-Kirchoff theory or geometrical optical approximation are exact solutions to Maxwell's equations. The strong agreement between the two simulation results in terms of the peak-trough structure and the number of relevant reflections indicate that the method used in this work provides both qualitative and quantitative information about wavefields propagating through capillary devices.

3. Results and discussion

To demonstrate the influence of the extended source on the device response, the ray locations at the device output are shown in Fig. 2 for different anode point positions. The ray output locations are strongly influenced by the anode point location, demonstrating that an experimentally significant anode size has been chosen. The ray locations are similar to those shown in previous simulation studies [27]. It is noteworthy that the ray locations alone do not provide the wavefield intensity and do not enable the evaluation of spatial coherence properties.

The intensity of the simulated output wavefield, computed in step 3, containing responses from all anode points is shown in Fig. 3. Additionally, the intensity of wavefields propagated away from the output plane, as computed in step 4 with a conventional Fresnel propagation operator, are shown. As the wavefields propagate away from the device, the intensity from the individual capillaries begins to diverge and overlap somewhat while the response from the overall device remains relatively collimated. This general behavior corresponds well with experimental results in the literature [37].
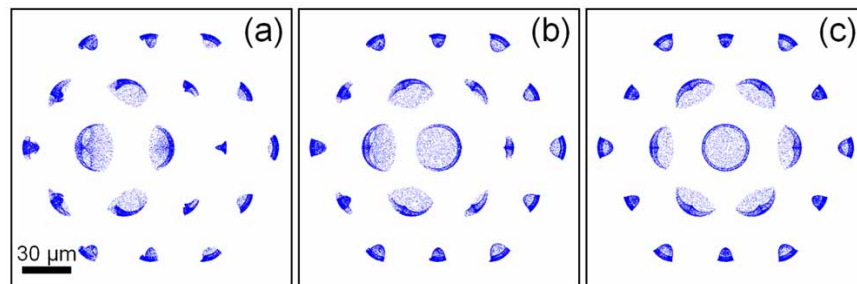

Fig. 2. Simulation results showing the spatial distribution of ray locations at the polycapillary device output plane with varying input anode source point locations. The panels show (from left to right) the anode source point locations (-6.4 μm, 0), (-3.2 μm, 0), and (0, 0).

Finally, the spectral degree of coherence, computed in step 5 from the wavefield responses of individual anode source points, or modes, is shown in Fig. 4. The two-point spectral degree of coherence is shown in each frame as an image with reference to a point $\mathbf{r}_1$ in the output plane. The simulated optic has a highly structured coherence response that, in the output plane, is characterized by several "bright spots" corresponding to a high spatial degree of correlation with $\mathbf{r}_1$. As the wavefields propagate away from the device, the structured spatial response begins
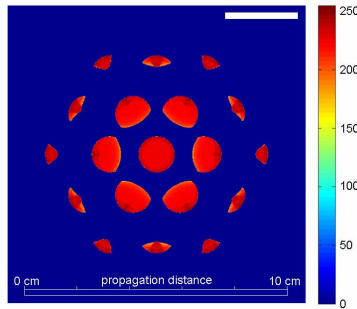
Fig. 3. Simulation results showing the log intensity of the polycapillary device wavefield output at distances ($d = 0$-10 cm with 0.5 cm increments) from the output plane (Media 1). As the wavefield propagates, the response from individual capillaries diverges and overlaps.

to disperse, causing a more uniform effective spectral degree of coherence of approximately $\mu_{\text{eff}} = 0.3$, especially when referenced to $r_1 = (0,0)$.
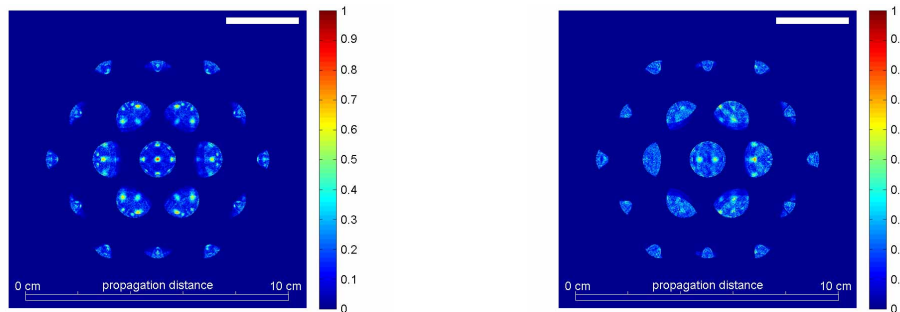

Fig. 4. Simulation results showing the spectral degree of coherence of the polycapillary device output wavefield. The spectral degree of coherence is a two-point quantity, and these data are shown as a function of r_2 with $r_1 = (0, 0)$ on the left (Media 2) and $r_1 = (63.8 \, \mu m, 0)$ on the right (Media 3). r_1 corresponds to the center point (left) and to the center point of the first capillary right of the center in the device output plane (right). Data are shown at distances ($d = 0$-10 cm with 0.5 cm increments) from the output plane.

This framework for the analysis of polycapillary device spatial coherence properties opens the door for more comprehensive investigations of the influence of device parameters on the coherence response and optimization of these parameters for specific applications. One potential application for collimating x-ray optics generally is in phase-contrast imaging techniques. In-line phase contrast methods, specifically, suffer from a trade-off between the source coherence necessary for generation of phase-contrast features and the source flux. Collimating optics can potentially alter this relationship by capturing a larger solid angle of an x-ray tube's output than would be possible otherwise. A key question, however, is how the wavefield coherence properties are changed due to propagation through the polycapillary device and the effect on image quality. The framework described here could potentially be used to evaluate the suitability of these devices for phase-contrast imaging. In addition, the simulation methods presented here may be useful for investigation of the wavefield output from polycapillary devices. Experimental measurements of these devices have demonstrated that the output intensity of certain devices contains ringing features that are strongly suggestive of the Fraunhofer diffraction patterns found due to light propagation through an aperture [17]. These effects are best character-

ized when the phase of propagating rays are accounted for in the output, especially as capillary devices are manufactured at smaller diameters where these patterns are most evident [18]. Interference effects, which are well known to occur in multiple-reflection optics [8, 16], may also be investigated with access to simulations of the wavefield without the need for an analytic solution to the wave equation.

The framework presented in this work consists of an adaptable five-step process. In future work, these steps may be altered to address specific topics of interest. For example, enhanced polycapillary device simulation methods may be incorporated into step 2. Specifically, the effects of capillary waviness and surface roughness have not been included here and may potentially have a substantial effect on the coherence properties of a device. In addition, a number of methods exist to perform the wavefield construction in step 3, the accuracy of which could form the basis of future studies. The methods presented here form the basis for improved understanding of the properties of polycapillary devices and provide a framework for future investigations into the effects of polycapillary optical devices on spatial coherence properties.

Acknowledgments